

Article

Ni_{0.6}Zn_{0.4}O Synthesised via a Solid-State Method for Promoting Hydrogen Sorption from MgH₂

Noratiqah Sazelee ¹, Muhamad Faiz Md Din ² and Mohammad Ismail ^{1,*}

¹ Energy Storage Research Group, Faculty of Ocean Engineering Technology and Informatics, University Malaysia Terengganu, Kuala Nerus 21030, Malaysia; atiqahsazelee19@gmail.com

² Department of Electrical and Electronic Engineering, Faculty of Engineering, National Defence University of Malaysia, Kem Sungai Besi, Kuala Lumpur 57000, Malaysia; faizmd@upnm.edu.my

* Correspondence: mohammadismail@umt.edu.my; Tel.: +60-9668-3487

Abstract: Magnesium hydrides (MgH₂) have drawn a lot of interest as a promising hydrogen storage material option due to their good reversibility and high hydrogen storage capacity (7.60 wt.%). However, the high hydrogen desorption temperature (more than 400 °C) and slow sorption kinetics of MgH₂ are the main obstacles to its practical use. In this research, nickel zinc oxide (Ni_{0.6}Zn_{0.4}O) was synthesized via the solid-state method and doped into MgH₂ to overcome the drawbacks of MgH₂. The onset desorption temperature of the MgH₂-10 wt.% Ni_{0.6}Zn_{0.4}O sample was reduced to 285 °C, 133 °C, and 56 °C lower than that of pure MgH₂ and milled MgH₂, respectively. Furthermore, at 250 °C, the MgH₂-10 wt.% Ni_{0.6}Zn_{0.4}O sample could absorb 6.50 wt.% of H₂ and desorbed 2.20 wt.% of H₂ at 300 °C within 1 h. With the addition of 10 wt.% of Ni_{0.6}Zn_{0.4}O, the activation energy of MgH₂ dropped from 133 kJ/mol to 97 kJ/mol. The morphology of the samples also demonstrated that the particle size is smaller compared with undoped samples. It is believed that in situ forms of NiO, ZnO, and MgO had good catalytic effects on MgH₂, significantly reducing the activation energy and onset desorption temperature while improving the sorption kinetics of MgH₂.

Keywords: metal oxide; nickel zinc oxide; magnesium hydride; solid-state hydrogen storage



Citation: Sazelee, N.; Md Din, M.F.; Ismail, M. Ni_{0.6}Zn_{0.4}O Synthesised via a Solid-State Method for Promoting Hydrogen Sorption from MgH₂. *Materials* **2023**, *16*, 2176. <https://doi.org/10.3390/ma16062176>

Academic Editors: Alessandro Dell'Era and Erwin Ciro Zuleta

Received: 9 February 2023
Revised: 23 February 2023
Accepted: 28 February 2023
Published: 8 March 2023



Copyright: © 2023 by the authors. Licensee MDPI, Basel, Switzerland. This article is an open access article distributed under the terms and conditions of the Creative Commons Attribution (CC BY) license (<https://creativecommons.org/licenses/by/4.0/>).

1. Introduction

Due to its enormous energy density (142 MJ/kg), abundance, and completely clean combustion, hydrogen is gaining more attention as an alternative energy carrier [1,2]. However, the limited availability of effective storage solutions has prevented the widespread use of hydrogen. The three conventional systems for storing hydrogen are cryogenic liquid storage (5–10 bar, 253 °C), compressed gas storage (350–700 bar at ambient temperature), and solid-state storage [3,4]. For solid-state storage, hydrogen can be stored in a chemical hydride such as ammonia borane [5,6] or in metal hydrides such as MgH₂, LiAlH₄, NaAlH₄, and other materials and is expected to have a high hydrogen capacity [7–9]. Nevertheless, MgH₂ is appealing because of its abundance of resources, cheapness, and high gravimetric capacity (7.60 wt.%) [10–12]. The practical applications for MgH₂ were still lacking because of sluggish kinetics, a high temperature (more than 400 °C), and a high dissociation enthalpy ($\Delta H = -74.5$ kJ/mol) [13,14]. Several attempts have been conducted to overcome the drawbacks of MgH₂, such as using the ball milling technique (to create smaller particles size) and doping with additives/catalysts including transition metals (Cu, Nb, Ti, Zn, Ni, and Co) and their compounds (likes carbides, fluorides, oxides and hydrides), nonmetallic materials (such as carbon nanotubes, graphene, carbon, and graphite), and intermetallics [15–18].

Ni is one of the effective catalysts for the MgH₂ system. A previous study revealed that by synthesizing the Ni@rGO catalyst, the desorption temperature of MgH₂ + 10 wt.% Ni₄@rGO₆ samples decreased by 61 °C [19]. Besides that, the MgH₂ + 10 wt.% Ni₄@rGO₆ samples are capable of absorbing 5.00 wt.% H₂ in 20 min at 100 °C and desorbing 6.10 wt.% of

H₂ at 300 °C within 15 min. A study led by Hou et al. [20] examined the role of NiMoO₄ as a catalyst through the milling process in enhancing the performance of hydrogen storage MgH₂. It is noteworthy that hydrothermal and sintering processes were used to produce NiMoO₄. According to the findings, the in situ formation of Mg₂Ni/Mg₂NiH₄ by NiMoO₄ and MgH₂ promotes the fast motion of hydrogen and boosts the hydrogen sorption performance of MgH₂. Meng and co-workers [21] synthesized Ni@C by electrospinning technique and found that the MgH₂-Ni@C samples released approximately 5.79 wt.% of H₂ at 280 °C and 6.12 wt.% of H₂ at 300 °C, whereas milled MgH₂ hardly decomposes under the same time frame. A previous study suggested a new method to analyze the impact of Ni nanopowder on the hydrogen storage performance of MgH₂, and it was found that within 10 min, MgH₂-2 mol% Ni could absorb 5.30 wt.% of H₂ at 300 °C [22].

Besides that, the formation of the reversible transition for Mg₂Ni/Mg₂NiH₄ is another significant point to be made based on the Mg-Ni system which revealed a positive catalytic effect of MgH₂ [23]. Another study stated that the in situ formation of Mg₂NiH₄ serves as a hydrogen pump to propel the absorption/desorption kinetics of MgH₂, hence boosting the hydrogen storage performance of MgH₂ [24]. This statement was also confirmed by Yang et al. [25]. According to Ying et al. [26], the Mg₂Ni phase served as a catalyst for the hydrogen molecule dissociation, causing faster nucleation of MgH₂. As reported by the deep-going Fu's group [27], the active species of Mg₂Ni/Mg₂NiH₄ during the heating process managed to improve the hydrogen sorption kinetics of MgH₂ via the addition of FeNi₂S₄. At 310 °C, the absorption kinetics of MgH₂ speed up after the addition of Ni and ZrO₂ [28]. The samples can absorb 6.10 wt.% of H₂, while sluggish kinetics can be observed for milled MgH₂ (4.60 wt.%). Furthermore, by the method of reducing self-assembled layered double hydroxide and graphene oxide to create NiCu/rGO, Lie et al. [29] demonstrated good hydrogen sorption kinetics compared with milled MgH₂. Mao and co-workers [30] exposed that MgH₂ with NiCl₂ shows better sorption properties than CoCl₂-doped samples. They found out that MgH₂/NiCl₂ decomposes at 300 °C while MgH₂/CoCl₂ decomposes at 304 °C. Furthermore, MgH₂/NiCl₂ composite released 4.58 wt.% of H₂ at 300 °C within 1 h, compared with 2.21 wt.% for MgH₂/CoCl₂ and 0.77 wt.% of H₂ for pure MgH₂.

Studies have pointed out another catalyst, which is Zinc (Zn) to accelerate the absorption/desorption kinetics of MgH₂. The onset desorption temperature of MgH₂ doped 3 mol% of ZnFe₂O₄ initiated at about 300 °C [31]. In addition, Polanski and Bystrzycki [32] observed that the addition of ZnO significantly accelerated the absorption kinetics at 325 °C in just 10 min and reduced the activation energy to 147 kJ/mol when compared with MgH₂. Thus, it is highly fascinating to explore the combination of these transition metals (Ni and Zn), given their good impact on boosting the absorption/desorption kinetics of hydrides. Furthermore, it is founded that the combination of several metals can speed up the hydrogen storage properties of MgH₂. Other researchers have exposed that adding 5 wt.% of Zr₇₀Ni₂₀Pd₁₀ powders to MgH₂ enhances the hydrogenation/dehydrogenation behaviors [33]. Accordingly, combining MgH₂ with additives/catalysts such as CeNi₅, NdNi₅, YNi₅, PrNi₅, and SmNi₅ showed faster absorption and desorption kinetics at 300 °C within 200 s and 1800 s, respectively [34]. El-Eskandarany et al. [35] came to the conclusion that adding the LaNi₃ additive caused a decrease in the initial decomposition temperature to 579 K and the activation energy to 73.26 kJ/mol. In addition, Wu et al. [36] synthesized porous LaNiO₃ using a precipitation-combustion method and found that 10 wt.% of LaNiO₃ can absorb 5.10 wt.% of H₂ within 60 s at 200 °C. The further study exposed that in situ formations of LaH₃ and Mg₂NiH₄ during the heating process significantly enhanced the performance of hydrogen storage for MgH₂.

Therefore, in this study, Ni_{0.6}Zn_{0.4}O was prepared by using the solid-state method. This additive was used in order to enhance the kinetics of absorption/desorption of MgH₂. This research is expected to reveal the catalytic mechanism to give a better understanding of the reaction between Ni_{0.6}Zn_{0.4}O and MgH₂. It is worth noting that Ni_{0.6}Zn_{0.4}O is first applied in MgH₂ for solid-state hydrogen storage performance.

2. Materials and Methods

For the first part, Ni_{0.6}Zn_{0.4}O was synthesized by the solid-state method by using Ni ($\geq 99\%$ pure; Sigma Aldrich, St. Louis, MO, USA), citric acid ($\geq 98\%$ pure; Sigma Aldrich), and zinc oxide (< 100 nm; Sigma Aldrich). All of these materials were ground together for 15 min using the following amounts: 0.1195 g of Ni, 0.1521 g of citric acid and 0.0326 g of zinc oxide. The sample was then calcined for 1 h at 1000 °C.

Next, Ni_{0.6}Zn_{0.4}O was used as an additive in order to improve the hydrogen storage performance of MgH₂. For this step, all the handling processes, including weighing, were completed in a glove box (MBRAUN UNIlab) with a pure argon atmosphere to prevent oxidation. The different weight percentages of Ni_{0.6}Zn_{0.4}O samples were milled together by using a planetary ball mill (NQM-0.4) to produce MgH₂-X wt.% Ni_{0.6}Zn_{0.4}O samples (where X = 5, 10, 15, and 20). In this experiment, commercial MgH₂ was acquired from Sigma Aldrich ($\geq 95\%$ pure). The sample was milled at 400 rpm for 1 h (15 min of milling time, 2 min of resting time, and 3 cycles) at room temperature. Each milling consists of four balls made of steel, and the ball-to-powder weight ratio is equal to 40:1.

To analyze the onset desorption temperature and absorption/desorption kinetics of the samples, Sievert-type pressure composition temperature (Advanced Materials Corporation, Pittsburgh, PA, USA) was used. The samples were heated up to 450 °C from room temperature. Meanwhile, 33.0 atm and 1.0 atm of pressure were used for the absorption/desorption kinetics process, which was carried out at 250 °C and 300 °C, respectively. The differential scanning calorimetry (DSC) was examined using a Mettler Toledo (Columbus, OH, USA) TG/DSC 1 in an Argon gas flow at 50 mL/min with various heating rates (15, 20, 25 and 30 °C/min) applied. About 3–5 mg of samples were loaded into an alumina crucible and heated from room temperature to 450 °C.

Structural characterization was performed with the help of the X-ray diffraction (XRD; Rigaku Miniflex, Tokyo, Japan) technique with a Cu-K α radiation range of 20–80° and a speed of 2.00°/min. The morphology of the composite was characterized by using scanning electron microscopy (SEM; JEOL JSM-6360LA) and energy dispersive X-ray spectroscopy (EDS; JEOL JSM-6360LA). The bonding of the samples was investigated using Fourier transform infrared spectroscopy (IR Shimadzu Tracer-100, Kyoto, Japan). Each FTIR data were obtained by averaging 40 scans from 400 to 2700 cm⁻¹, and Renishaw Raman spectroscopy was conducted at room temperature with a 0.1% power laser measurement. Pure MgH₂ and milled MgH₂ were also characterized by using all the instruments to compare the results between the samples.

3. Results and Discussion

The XRD spectra of Ni_{0.6}Zn_{0.4}O samples prepared by the solid-state method are presented in Figure 1a. Referring to the reported standard Ni_{0.6}Zn_{0.4}O sample (JCPDF 75-0273), all reported diffraction peaks match it perfectly. Zinc oxide and nickel oxide, two potential impurity phases, were not found in the XRD spectra. The diffraction peaks at 36.85°, 42.81°, 62.15°, 74.49°, and 78.42° are used to represent the Ni_{0.6}Zn_{0.4}O crystal planes (111), (200), (220), (311), and (222), respectively. Similar observations were reported by Wei and co-workers [37]. The crystallite sizes (L) are estimated at 11.24 nm through the Scherrer formula as in Equation (1) below:

$$L = K\lambda/\beta \cos \theta \quad (1)$$

where λ is the X-ray used (0.154 nm), β (physical broadening) is the full width at half the maximum, θ is the angle of Bragg's diffraction, and shape factor $K = 0.94$ constant. Figure 1b depicts the FTIR spectra of Ni_{0.6}Zn_{0.4}O, and the peaks at 418 cm⁻¹ correspond to the Ni–O bond as suggested in the previous study [38,39]. Meanwhile, the peaks at 502 cm⁻¹ are attributed to the Zn–O peaks as indicated by Raja et al. [40] and Handore et al. [41]. Furthermore, Raman spectra of Ni_{0.6}Zn_{0.4}O samples were present as in Figure 1c, clearly showing 3 distinct Raman bands. The peaks at 351 cm⁻¹ and 401 cm⁻¹ were attributed to

the Zn–O peak, as proven by Bhunia et al. [42] and Marinho et al. [43]. Meanwhile, the peak at 481 cm^{-1} matches the Ni–O peak as exposed by Bose et al. [44].

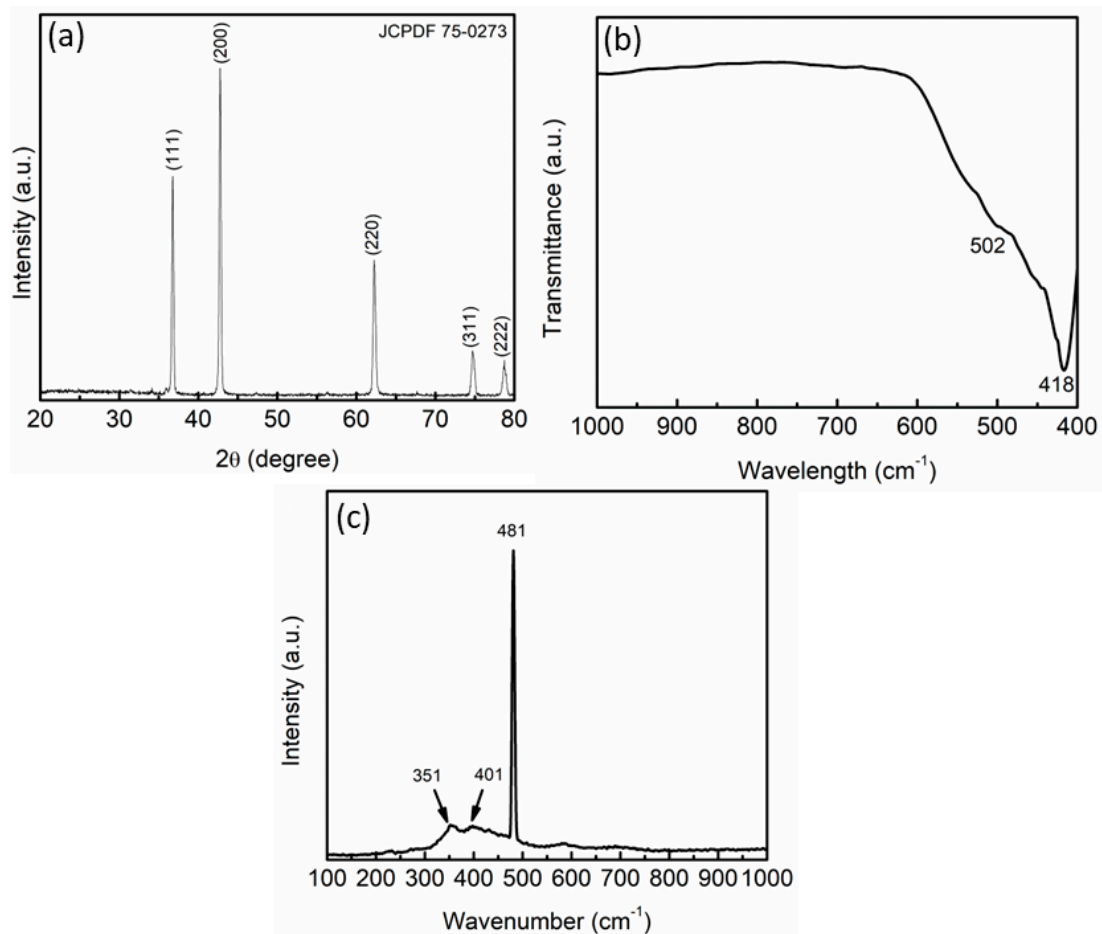


Figure 1. (a) XRD pattern, (b) FTIR spectra and (c) Raman spectra of $\text{Ni}_{0.6}\text{Zn}_{0.4}\text{O}$.

EDS characterization for $\text{Ni}_{0.6}\text{Zn}_{0.4}\text{O}$ was conducted as shown in Figure 2 in order to recognize the existence and distribution of $\text{Ni}_{0.6}\text{Zn}_{0.4}\text{O}$. To evaluate the element distribution over a broad region, the magnification was set at $500\times$. The EDS mapping below shows the distribution of different elements. Figure 2a displays the $\text{Ni}_{0.6}\text{Zn}_{0.4}\text{O}$ samples; Figure 2b,c show the Ni and Zn elements, respectively. However, Figure 2d illustrates the O element. From the result obtained, it is shown that elements Ni, Zn, and O are uniformly distributed. Table 1 below proved the element of the $\text{Ni}_{0.6}\text{Zn}_{0.4}\text{O}$. From the results of XRD, FTIR, Raman, and EDS mapping, it is proved that pure $\text{Ni}_{0.6}\text{Zn}_{0.4}\text{O}$ was successfully synthesized by the solid-state method. The SEM images as presented in Figure 2e indicated that $\text{Ni}_{0.6}\text{Zn}_{0.4}\text{O}$ has a spherical morphology and the particles were agglomerate. Meanwhile, Figure 2f shows the results of the particle size distribution (PSD) analysis. The PSD was analyzed using Image J. Most of the particles are concentrated at a size of approximately $98.6\ \mu\text{m}$.

Figure 3a exhibited the temperature-programmed desorption curves of pure MgH_2 , milled MgH_2 , and MgH_2 doped with different weight percentages (5, 10, 15, and 20) of $\text{Ni}_{0.6}\text{Zn}_{0.4}\text{O}$. The pure MgH_2 decomposes at $418\text{ }^\circ\text{C}$ with an approximate 7.10 wt.% total dehydrogenation capacity. Milling MgH_2 for 1 h lowered the onset desorption temperature to $341\text{ }^\circ\text{C}$, $77\text{ }^\circ\text{C}$ lower than pure MgH_2 . Remarkably, the onset desorption temperature reduces after the $\text{Ni}_{0.6}\text{Zn}_{0.4}\text{O}$ additive is added. MgH_2 -5 wt.% $\text{Ni}_{0.6}\text{Zn}_{0.4}\text{O}$ samples decompose at $280\text{ }^\circ\text{C}$ with a 6.80 wt.% total H_2 release. After the addition of 10 wt.%, 15 wt.%, and 20 wt.% of $\text{Ni}_{0.6}\text{Zn}_{0.4}\text{O}$ as an additive with MgH_2 , the initial desorption temperatures were lowered to $285\text{ }^\circ\text{C}$, $305\text{ }^\circ\text{C}$, and $293\text{ }^\circ\text{C}$, respectively. In addition, as the amount of

$\text{Ni}_{0.6}\text{Zn}_{0.4}\text{O}$ increased to 10 wt.%, 15 wt.% and 20 wt.%, the total hydrogen release declined to 6.80 wt.%, 6.50 wt.% and 6.30 wt.%, respectively. Numerous studies have shown that this trend was caused by the dead weight of the $\text{Ni}_{0.6}\text{Zn}_{0.4}\text{O}$. Research conducted by Bhatnagar et al. [45] stated that the total desorption capacity of $\text{MgH}_2\text{-TiF}_2$ is less than MgH_2 because TiH_2 somehow does not evolve H_2 and acts as a dead weight for the $\text{MgH}_2\text{-TiH}_2$ system.

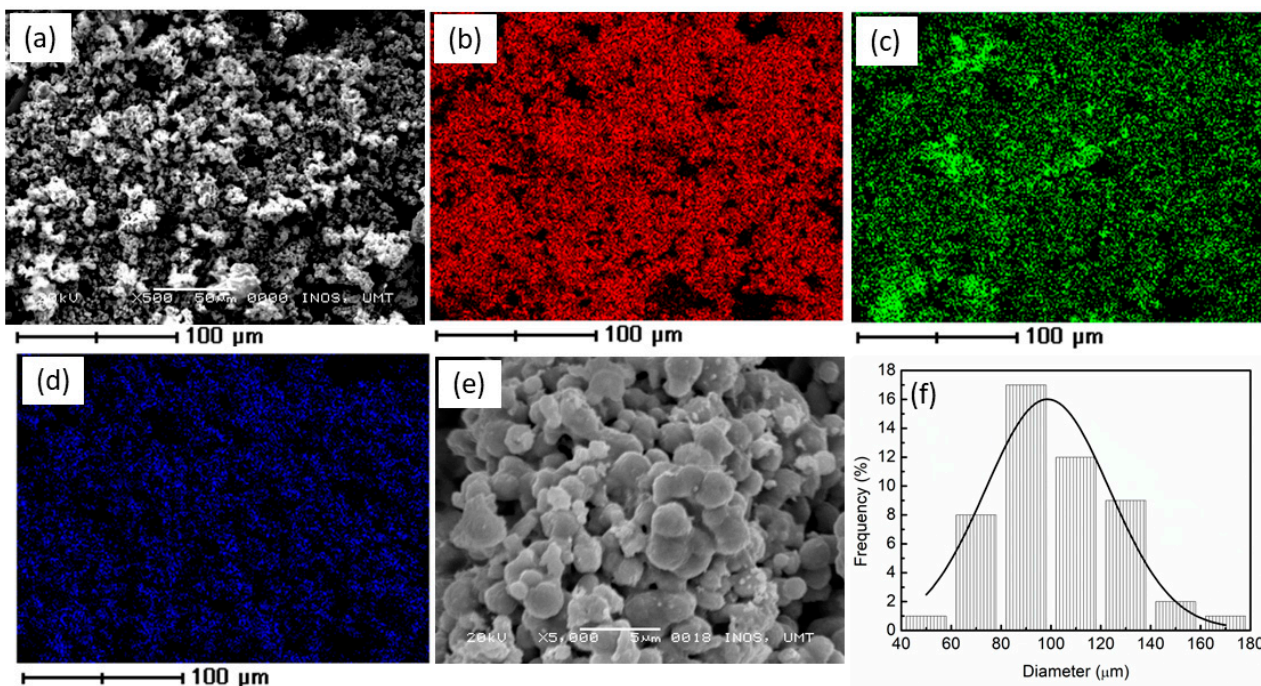


Figure 2. EDS images of the (a) $\text{Ni}_{0.6}\text{Zn}_{0.4}\text{O}$, (b) Ni, (c) Zn, (d) O, (e) SEM images and (f) Particle size distribution of $\text{Ni}_{0.6}\text{Zn}_{0.4}\text{O}$.

Table 1. Element of $\text{Ni}_{0.6}\text{Zn}_{0.4}\text{O}$ samples.

Element	Mass (%)
Ni	61.88
Zn	17.08
O	21.04
Total	100.00

The absorption kinetics was conducted at 250 °C for 1 h, and the result also shows that the addition of the $\text{Ni}_{0.6}\text{Zn}_{0.4}\text{O}$ additive enhances the performance of MgH_2 , as proved in Figure 3b. The results showed that within only 5 min, milled MgH_2 was able to absorb 4.80 wt.% of H_2 . The addition of 10 wt.%, and 15 wt.% of $\text{Ni}_{0.6}\text{Zn}_{0.4}\text{O}$ with MgH_2 increased their absorption capacity to 6.50 wt.% of H_2 in the same amount of time. A slight increment in the absorption capacity for $\text{MgH}_2\text{-20 wt.% Ni}_{0.6}\text{Zn}_{0.4}\text{O}$ samples can be observed, which is 5.40 wt.%. However, $\text{MgH}_2\text{-5 wt.% Ni}_{0.6}\text{Zn}_{0.4}\text{O}$ samples showed the lowest amount of absorption capacity, which is 4.10 wt.% under the same circumstances. The absorption kinetics of MgH_2 with another catalyst were also included for comparison purposes, as shown in Table 2.

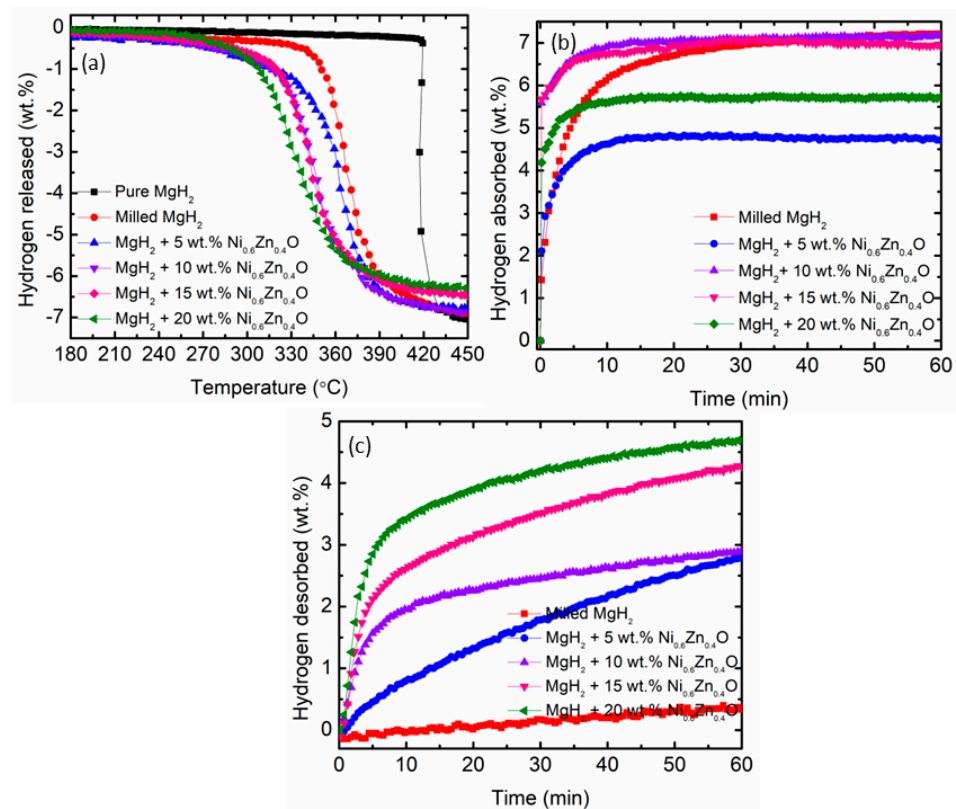


Figure 3. (a) Temperature-programmed-desorption curves, (b) Absorption kinetics at 250 °C, 33.0 atm and (c) Desorption kinetics at 300 °C, 1.0 atm.

Table 2. Isothermal absorption kinetics curves from previous studies.

System	Temperature for Isothermal Absorption Kinetics (°C)	Absorption Capacity (wt.%)	Time (Min)	Refs.
MgH ₂ + 10 wt.% BaFe ₁₂ O ₁₉	150	4.30	10	[46]
MgH ₂ + 10 wt.% MgFe ₂ O ₄	200	5.50	10	[47]
MgH ₂ + 10 wt.% Co ₂ NiO	320	2.50	1.7	[48]
MgH ₂ + Ni-50% Cu	300	5.24	30	[49]
MgH ₂ -10 wt.% Ni _{0.6} Zn _{0.4} O	250	6.50	60	(this work)

Apart from the absorption behavior of undoped and doped samples, the hydrogen desorption kinetics of MgH₂ doped with Xwt.% Ni_{0.6}Zn_{0.4}O (where X = 5, 10, 15, and 20) were conducted at 300 °C for 1 h, as shown in Figure 3c. It is apparent that MgH₂ doped with Ni_{0.6}Zn_{0.4}O desorbed hydrogen significantly faster than that of milled MgH₂. Milled MgH₂ can desorb 0.02 wt.% of H₂ while MgH₂ doped with 5 wt.% of Ni_{0.6}Zn_{0.4}O can desorb 1.30 wt.% of H₂, and MgH₂-10 wt.% Ni_{0.6}Zn_{0.4}O samples desorbed 2.30 wt.% of H₂ within 20 min. As the Ni_{0.6}Zn_{0.4}O additive is increased to 15 wt.% and 20 wt.%, the total amount of hydrogen released rises to 3.10 wt.% and 3.90 wt.%, respectively.

The good catalytic effect of the Ni_{0.6}Zn_{0.4}O were clarified by the faster absorption/desorption kinetics of MgH₂. According to Yang et al. [25], the Mg–H bond was significantly stretched by the Ni catalyst action, which is more favorable for H separation and can speed up the desorption rate of MgH₂. It is clearly apparent that introducing Ni_{0.6}Zn_{0.4}O as an additive will significantly reduce the onset desorption temperature and enhance the absorption/desorption kinetics of MgH₂ as summarized in Table 3 below. Pure MgH₂ and milled MgH₂ were also included for comparison. Considering the influence of the Ni_{0.6}Zn_{0.4}O as an additive on the onset desorption temperature and sorption kinetics, MgH₂-10 wt.% Ni_{0.6}Zn_{0.4}O samples as an additive were selected for further study.

Table 3. Onset desorption temperature, absorption capacity at 250 °C for 5 min and desorption capacity at 300 °C for 1 h.

	Onset Desorption Temperature (°C)	Absorption Capacity (wt.%)	Desorption Capacity (wt.%)
Pure MgH ₂	418	-	-
Milled MgH ₂	341	4.8	0.3
MgH ₂ -5 wt.% Ni _{0.6} Zn _{0.4} O samples	280	4.1	2.7
MgH ₂ -10 wt.% Ni _{0.6} Zn _{0.4} O samples	285	6.5	2.9
MgH ₂ -15 wt.% Ni _{0.6} Zn _{0.4} O samples	305	6.5	4.3
MgH ₂ -20 wt.% Ni _{0.6} Zn _{0.4} O samples	293	5.4	4.7

Using kinetic models to represent the behavior of absorption and desorption is a great idea to gain a better understanding of the kinetic mechanism in MgH₂-10 wt.% Ni_{0.6}Zn_{0.4}O samples. In 2010, Luo et al. [50] investigated two kinds of kinetic models, which are the Jander model and the Chou model, on the hydriding kinetics of Mg-Ni based alloys. For instance, Cheng et al. [51] proposed a kinetic model based on the characteristics of desorption time for TiVNbCr alloy using the Jander diffusion model, the Ginstling-Brounshtein model, and the Johnson-Mehl-Avrami-Kolmogorov (JMA) equation. Furthermore, JMA plots of the Mg₉₀Ce₅Y₅ alloy with various catalysts such as MoO₃, MoO₂, and Mo were explored by Wang and co-workers [52]. In this study, the kinetic models of JMA and Contracting Volume (CV) were analyzed as can be seen in Table 4 [53]. According to Pang and Li [54], these models were chosen because they accurately fit the experimental data and did not require any additional approximations or assumptions. Additionally, these models have been used by other researchers to comprehend the rate-limiting steps of the material.

Table 4. Equation for kinetic models used for absorption and desorption kinetics of this study.

Integrated Equation	Model
$A = kt$	Surface-controlled (chemisorption)
$[-\ln(1 - \alpha)]^{1/2} = kt$	JMA, $n = 2$ (e.g., two-dimensional growth of existing nuclei with constant interface velocity)
$[-\ln(1 - \alpha)]^{1/3} = kt$	JMA, $n = 3$ (e.g., two-dimensional growth of existing nuclei with constant interface velocity)
$1 - (1 - \alpha)^{1/3} = kt$	CV 2D: contracting volume, three-dimensional growth with constant interface velocity
$1 - (2\alpha/3) - (1 - \alpha)^{2/3} = kt$	CV 3D: contracting volume, three-dimensional growth diffusion controlled with decreasing interface velocity

Where t is time, k is a reaction rate constant and α is reacted fraction.

In this context, the best linear plot of the absorption and desorption kinetics of MgH₂-10 wt.% Ni_{0.6}Zn_{0.4}O samples with the kinetic equations in Table 4 determined the rate-limiting steps as shown in Figure 4a,b, respectively. The kinetic curves for the samples were measured for the reacted fraction in the range of 0 to 80%. As shown in the following figure, the CV 3D decrease surface can best explain the absorption and desorption kinetics at 250 °C and 300 °C, respectively.

The DSC curves for milled MgH₂ and MgH₂-10 wt.% Ni_{0.6}Zn_{0.4}O samples were evaluated at different heating rates, as represented in Figure 5a and 5b, respectively. One endothermic peak is visible in both samples, indicating the decomposition of MgH₂ to Mg. Increasing the heating rates resulted in an increase in the temperature of the samples. For comparison, DSC traces at 20 °C/min for milled MgH₂ and MgH₂-10 wt.% Ni_{0.6}Zn_{0.4}O samples were examined as in Figure 5c. From the result obtained, the temperature for milled MgH₂ was 428 °C, while the MgH₂-10 wt.% Ni_{0.6}Zn_{0.4}O samples were 397 °C. It is noticeable that the Ni_{0.6}Zn_{0.4}O additive affected the endothermic peak of hydrogen desorption to shift remarkably to a lower temperature. Besides, it was observed that the

inclusion of Mg(Nb)O resulted in a reduction in the endothermic peak of MgH₂, which is due to the weakening of Mg–H bonds caused by Mg(Nb)O [55].

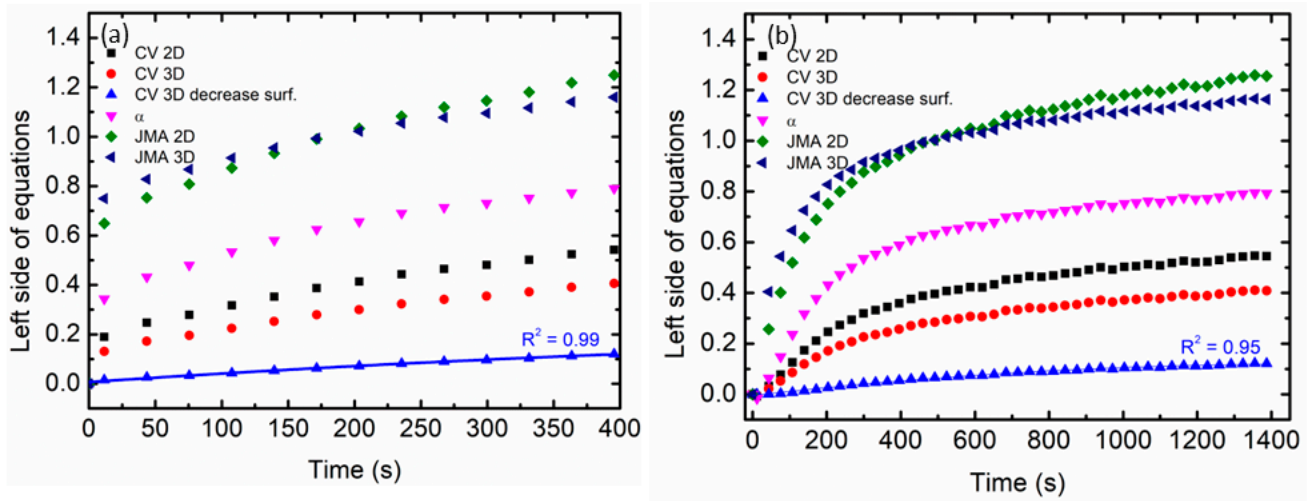


Figure 4. The calculation of the various kinetic equations for MgH₂–10 wt.% Ni_{0.6}Zn_{0.4}O samples is shown in Table 4 for (a) absorption kinetics at 250 °C and (b) desorption kinetics at 300 °C.

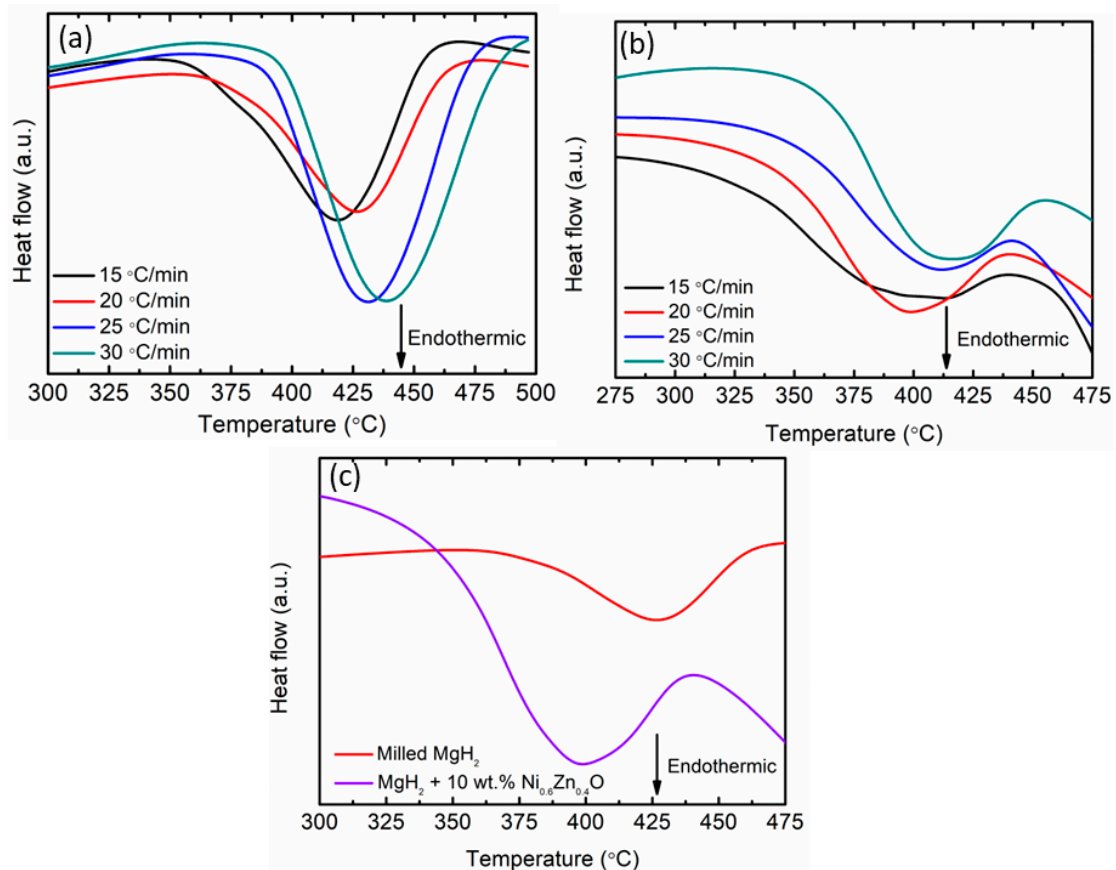


Figure 5. DSC traces for (a) milled MgH₂, (b) MgH₂–10 wt.% Ni_{0.6}Zn_{0.4}O samples at 15, 20, 25 and 30 °C/min and (c) DSC traces at 20 °C/min for milled MgH₂ and MgH₂–10 wt.% Ni_{0.6}Zn_{0.4}O samples.

The remarkable effect of the $\text{Ni}_{0.6}\text{Zn}_{0.4}\text{O}$ additive on the desorption kinetic properties of MgH_2 was further examined by calculating the apparent activation energy (E_A) using the Kissinger equation below (Equation (2)):

$$\ln [\beta/T_p^2] = -E_A/RT_p + A \quad (2)$$

where T_p is the peak temperature in the DSC curve, β is the heating rate of the samples, R is the gas constant, and A is a linear constant. Figure 6 revealed the Kissinger plots of the milled MgH_2 and MgH_2 -10 wt.% $\text{Ni}_{0.6}\text{Zn}_{0.4}\text{O}$ samples by fitting the data points. From the figure, the activation energy of milled MgH_2 was 133 kJ/mol. However, in MgH_2 -10 wt.% $\text{Ni}_{0.6}\text{Zn}_{0.4}\text{O}$ samples, the value was reduced to 97 kJ/mol. This number dropped by 36 kJ/mol. This revealed that the addition of $\text{Ni}_{0.6}\text{Zn}_{0.4}\text{O}$ as an additive to MgH_2 resulted in a notable decrease in the kinetic barrier desorption of the MgH_2 system, which is beneficial for hydrogen release from MgH_2 . These findings are also consistent with earlier research that showed the addition of an additive or catalyst lowers the activation energy of MgH_2 [56,57]. Zhang and co-workers [58] exposed that the reaction energy barrier for the desorption reduced to 109 kJ/mol when MnMoO_4 was doped to MgH_2 . The apparent activation energy is roughly 30% lower than pure MgH_2 . According to research by Hu et al. [59], the addition of $\text{K}_2\text{Ti}_8\text{O}_{17}$ can successfully lower the activation energy by 59 kJ/mol.

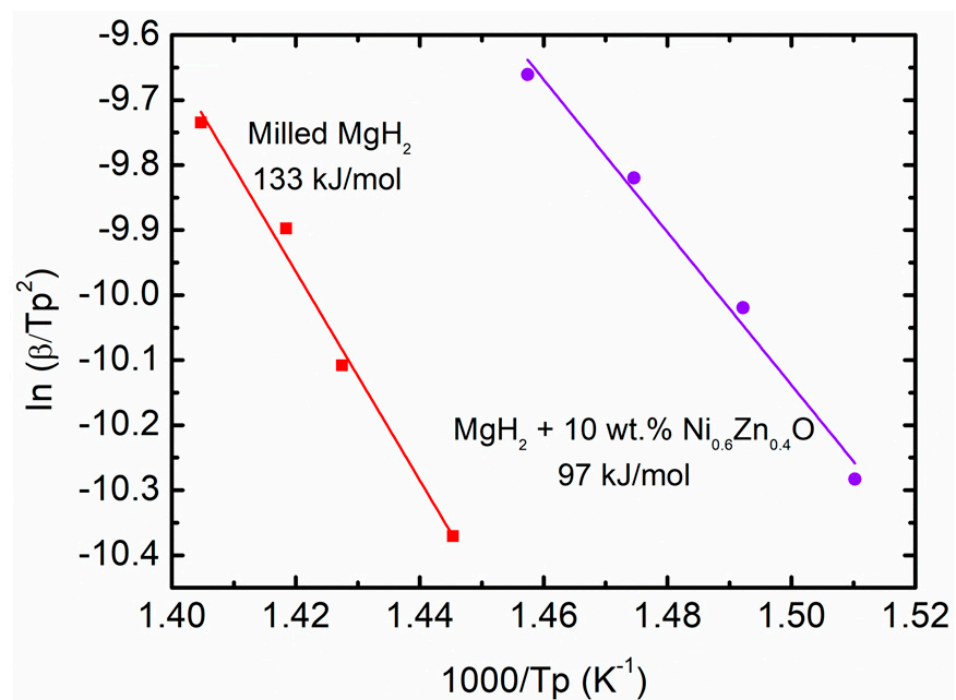


Figure 6. Activation energy for milled MgH_2 and MgH_2 -10 wt.% $\text{Ni}_{0.6}\text{Zn}_{0.4}\text{O}$ samples.

Figure 7 below displays SEM images of the pure MgH_2 , milled MgH_2 , and MgH_2 -10 wt.% $\text{Ni}_{0.6}\text{Zn}_{0.4}\text{O}$ samples. Pure MgH_2 revealed the morphology of the sample as an irregular shape range larger than $50\ \mu\text{m}$ as in Figure 7a. A similar outcome was discovered by Mahsa et al. [60]. They exposed that the morphology of pure MgH_2 has irregular shapes with larger particles. It should be noted that smaller particle sizes can be observed after MgH_2 is milled for 1 h, as presented in Figure 7b. This proved that the performance of MgH_2 was also directly affected by the milling process. Next, changes in the morphological parameters of the powder can also be detected by Czujko et al. [61]. According to Shahi et al. [62], the onset desorption temperature of pure MgH_2 decreased from $422\ ^\circ\text{C}$ to $367\ ^\circ\text{C}$. It may be pointed out that the milling process of MgH_2 for 25 h reduces the particle size of MgH_2 , thereby lowering the desorption temperature of MgH_2 . As expected, MgH_2 -10 wt.%

$\text{Ni}_{0.6}\text{Zn}_{0.4}\text{O}$ samples exhibited a smaller particle size as compared with milled MgH_2 (as can be seen in Figure 7c). Ali et al. [56] introduced CoTiO_3 to MgH_2 and showed that the particle size of the composite changed to a finer and smaller size. According to the research results of Somo et al. [63], smaller particle sizes allow quick dissociation into the surface of materials. Besides that, the addition of Nb to MgH_2 creates a large number of hydrogen diffusion channels and speeds up hydrogen flow along the MgH_2/Mg interfaces, continuing to improve the sorption kinetics of MgH_2 [64]. In light of this, it is obvious that adding $\text{Ni}_{0.6}\text{Zn}_{0.4}\text{O}$ causes the particle size to be greatly decreased, which is useful for improving the performance of MgH_2 .

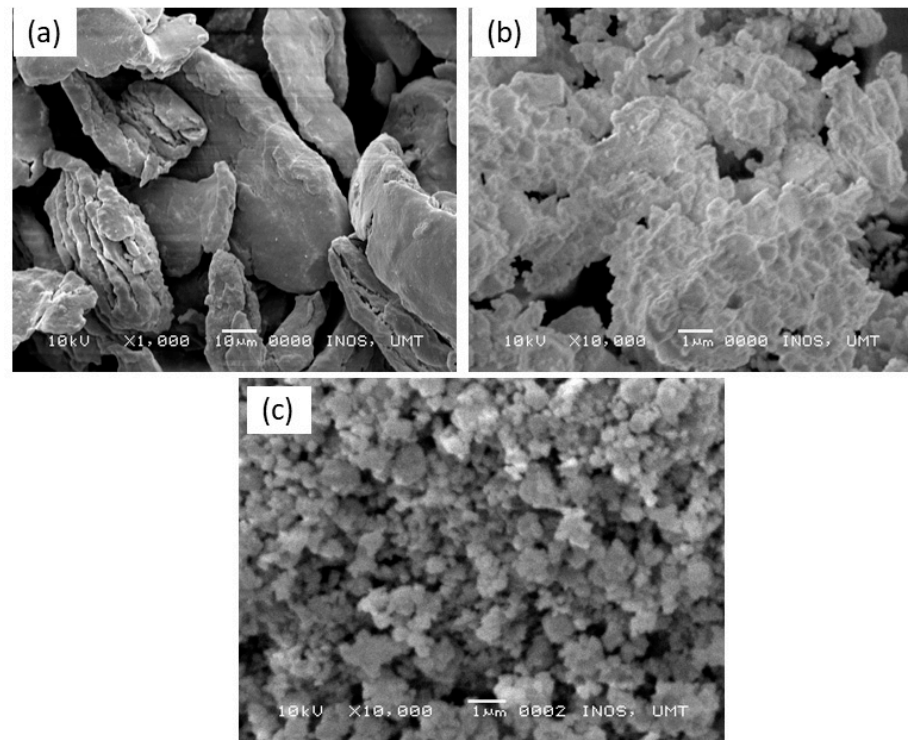


Figure 7. SEM images of (a) pure MgH_2 , (b) milled MgH_2 and (c) MgH_2 –10 wt.% $\text{Ni}_{0.6}\text{Zn}_{0.4}\text{O}$ samples.

The PSD of pure MgH_2 , milled MgH_2 , and MgH_2 –10 wt.% $\text{Ni}_{0.6}\text{Zn}_{0.4}\text{O}$ samples were analyzed using Image J (version 2022). As shown in Figure 8a, the PSD calculated for pure MgH_2 was 84.8 μm . The calculated PSD for milled MgH_2 decreased to 0.29 μm as shown in Figure 8b. A study led by Maddah et al. [65] exposed that the average particle size of MgH_2 decreased from 30 μm to 2.2 μm . Furthermore, as the milling time is extended up to 30 h, no discernible difference is seen. However, in this study, the PSD was decreased to 0.13 μm when 10 wt.% of $\text{Ni}_{0.6}\text{Zn}_{0.4}\text{O}$ was added to MgH_2 , as shown in Figure 8c. This demonstrated how significantly MgH_2 's size was reduced after the addition of $\text{Ni}_{0.6}\text{Zn}_{0.4}\text{O}$ as an additive. Moreover, Xiao and colleagues [66] stated that the particle size of milled MgH_2 decreased to a range of 80 to 80 nm and lowered to 50 to 400 nm after LiCl was added.

The effect of $\text{Ni}_{0.6}\text{Zn}_{0.4}\text{O}$ addition on the MgH_2 bonding was investigated by using FTIR, as shown in Figure 9. All the samples exhibited two bands: (i) 400–800 cm^{-1} , corresponding to Mg–H bending bands, and (ii) 800–1400 cm^{-1} , attributed to the Mg–H stretching bands as previously shown by Zhang et al. [67]. For milled MgH_2 , an obvious peak around 515 cm^{-1} is attributed to Mg–H bending bands. This peak indicated that the milled MgH_2 was stable during the milling process. In our study, the bending and stretching bands were at about 772 cm^{-1} and 1380 cm^{-1} , respectively. No new peak was detected due to the low amount of $\text{Ni}_{0.6}\text{Zn}_{0.4}\text{O}$ as an additive. However, after the addition of 10 wt.% $\text{Ni}_{0.6}\text{Zn}_{0.4}\text{O}$ as an additive, the peaks were shifted to a low wavenumber, which

indicates the weakness of the Mg–H bond. Furthermore, Ismail et al. [68] also agreed with these findings.

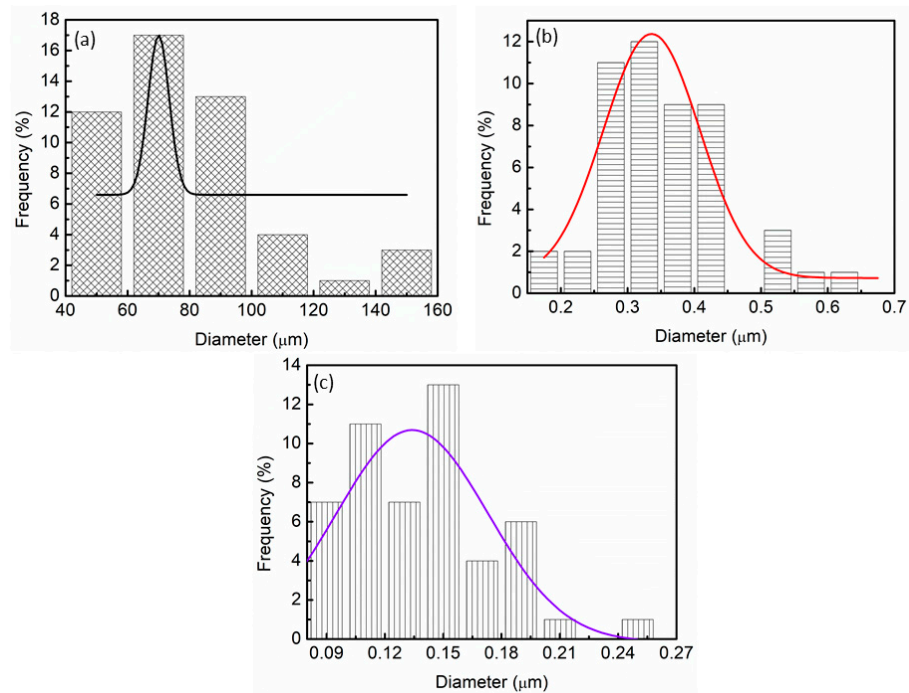


Figure 8. PSD of (a) pure MgH_2 , (b) milled MgH_2 and (c) MgH_2 –10 wt.% $\text{Ni}_{0.6}\text{Zn}_{0.4}\text{O}$ samples.

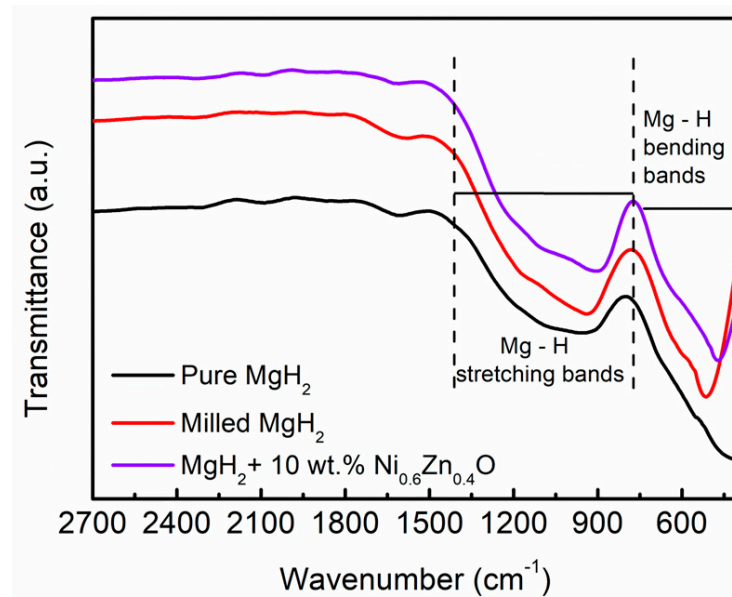
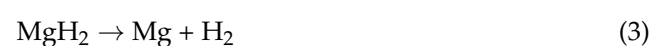


Figure 9. FTIR pattern of (a) pure MgH_2 , (b) milled MgH_2 and (c) MgH_2 –10 wt.% $\text{Ni}_{0.6}\text{Zn}_{0.4}\text{O}$ samples.

The XRD pattern of the MgH_2 –10 wt.% $\text{Ni}_{0.6}\text{Zn}_{0.4}\text{O}$ samples after milling for 1 h, after desorption at 450°C , and after absorption at 250°C at the 1st cycle is exhibited in Figure 10a. As shown in Figure 10, the peaks of $\text{Ni}_{0.6}\text{Zn}_{0.4}\text{O}$ and MgH_2 were present, which indicates the parent materials of the composite. Meanwhile, after MgH_2 –10 wt.% $\text{Ni}_{0.6}\text{Zn}_{0.4}\text{O}$ samples were heated at 450°C , as exhibited in the figure below (labelled desorption), the peaks of MgH_2 and $\text{Ni}_{0.6}\text{Zn}_{0.4}\text{O}$ disappeared. Peak Mg was present, which revealed that MgH_2 was fully decomposed to Mg as exhibited in the equation below:



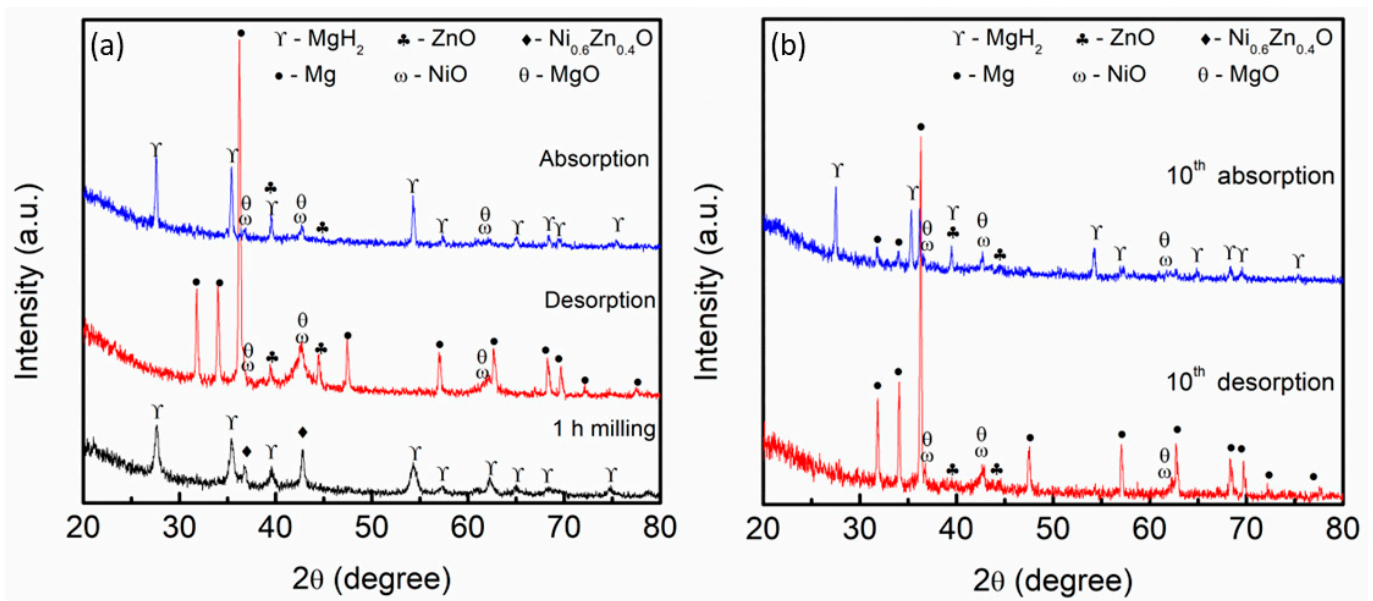


Figure 10. XRD pattern of MgH_2 -10 wt.% $\text{Ni}_{0.6}\text{Zn}_{0.4}\text{O}$ samples (a) after 1st cycle and (b) after 10th cycle.

New peaks of ZnO, NiO, and MgO could also be seen as the samples were heated up. However, the peaks of Mg were completely transformed into MgH_2 during the absorption process at 250 °C, while the peaks of ZnO, NiO, and MgO remained unaltered (labeled absorption).

The XRD pattern for MgH_2 -10 wt.% $\text{Ni}_{0.6}\text{Zn}_{0.4}\text{O}$ samples after the 10th cycle of desorption and absorption was analyzed and illustrated as in Figure 10b. Obviously, the Mg peak dominates even at the 10th cycle, and no peak of MgH_2 was found, as demonstrated in the figure below (labeled 10th desorption). However, the peaks of ZnO, NiO, and MgO remained unchanged even after the 10th cycle. Another peak of the XRD spectra for absorption at 10th cycles was also reported in Figure 10b below, labeled 10th absorption. The peaks of MgH_2 were found, which revealed the Mg peaks were transformed into MgH_2 . Nevertheless, the in situ forms of ZnO, NiO, and MgO still appeared and remain unchanged. Based on the result obtained, the in situ formation may also provide a significant effect that will help boost the hydrogen sorption performance of MgH_2 .

A previous work discovered that the performance of hydrogen storage MgH_2 is significantly improved by the inclusion of metal oxide as a catalyst or additive [69]. According to a study by Zou et al. [70], the polarization might weaken the Ti–O bonds and Mg–H bonds, which make MgH_2 decompose quickly after the addition of TiO. Furthermore, Huang et al. [71] discovered that faster absorption/desorption kinetics of MgH_2 can be observed after the addition of Sc_2O_3 and TiO_2 . Further findings indicate that the surface defects and grain boundaries created by the milling process after the addition of Sc_2O_3 and TiO_2 provide a significant number of diffusion channels and active sites that greatly enhance the kinetics of MgH_2 .

In this study, the in situ formation of MgO, NiO, and ZnO was observed during the heating process of MgH_2 -10 wt.% $\text{Ni}_{0.6}\text{Zn}_{0.4}\text{O}$ samples. The formation of MgO after the addition of additive/catalysts has well agreed with previous research. Aguey-Zinsou et al. [72] indicated that the role of MgO is rationalized in the concept of a “Process Control Agent”. On top of that, MgO has dispersed properties and good lubricant thus preventing MgH_2 from clumping together. Additionally, Shan et al. [73] also revealed that one of the final reaction products of CoFe_2O_4 and MgH_2 is MgO, which may help reduce the onset desorption temperature from 440 °C for as-received MgH_2 to 160 °C after doping with 7 mol% of CoFe_2O_4 . In order to tailor MgH_2 performance, Ali et al. [74] introduced 10 wt.% of MgNiO_2 to MgH_2 , and the results show that MgH_2 -10 wt.% MgNiO_2 samples

can desorb roughly 5.10 wt.% of H₂ within 10 min at 320 °C and begin to decompose at 258 °C. Surprisingly, at 200 °C, MgH₂–10 wt.% MgNiO₂ samples continue to absorb 6.10 wt.% of H₂ in just 10 min. The performance of MgH₂ as a hydrogen storage material is boosted by the formation of new MgO and NiO compounds.

A previous study reported that adding a Co₂NiO catalyst can lower the desorption temperature by 117 °C (pure MgH₂) and 70 °C (milled MgH₂) and decrease the activation energy by 65 kJ/mol and 15 kJ/mol for pure MgH₂ and milled MgH₂, respectively [48]. According to a study by Zhang et al. [75], the bond between Mg and H is weaker than the bond between transition metals such as Ni. The release of the H atom and H₂ recombination from the MgH₂ surface is encouraged by the weakening of the bond between H and Mg caused by the strong bonding between Ni and H. Besides, Patah et al. [76] also exposed the fact that adding ZnO to MgH₂ reduces the onset desorption peak of the DSC curves from 375 °C to 360 °C. Along this line, it is valuable to conclude that the addition of Ni_{0.6}Zn_{0.4}O as an additive significantly enhances the sorption properties of MgH₂. A study on the catalytic mechanism revealed that in situ formations of metal oxides such as MgO, ZnO, and NiO during the heating process may help in improving the hydrogen storage performance of MgH₂.

4. Conclusions

In this work, Ni_{0.6}Zn_{0.4}O samples were successfully synthesized via the solid-state method, and the catalytic effects of Ni_{0.6}Zn_{0.4}O on the hydrogen storage performance of MgH₂ were systematically studied for the first time. Different weight percentages (5, 10, 15, and 20 wt.%) of Ni_{0.6}Zn_{0.4}O were milled together for 1 h, and the onset desorption temperature was reduced to a range of 280 °C to 305 °C, which is lower than pure MgH₂ (418 °C) and milled MgH₂ (341 °C). The absorption and desorption kinetics of MgH₂ could be largely enhanced by the addition of 10 wt.% of Ni_{0.6}Zn_{0.4}O as an additive. The MgH₂–10 wt.% Ni_{0.6}Zn_{0.4}O samples can absorb 6.50 wt.% of H₂ in 1 h at 250 °C. Meanwhile, milled MgH₂ can absorb only 4.10 wt.% of H₂ under the same circumstances. For the desorption kinetics, the MgH₂–10 wt.% Ni_{0.6}Zn_{0.4}O samples can release approximately 2.20 wt.% of H₂ in 1 h at 300 °C, whereas pure MgH₂ and milled MgH₂ can only release releases <1.0 wt.% of H₂ under the same conditions. From DSC and Kissinger desorption analyses, the apparent activation energy of the MgH₂–10 wt.% Ni_{0.6}Zn_{0.4}O samples is 97 kJ/mol, resulting in a decrease of 36 kJ/mol compared with milled MgH₂. Furthermore, the morphology becomes smaller and less agglomerated after the addition of 10 wt.% Ni_{0.6}Zn_{0.4}O. Smaller particles size provided more grain boundaries and larger surface area which benefited the diffusion path for hydrogen during the absorption and release process. From these results, it can be concluded that the reduction in particle size and the in situ generated (ZnO, NiO, and MgO) during the heating process played synergistic catalytic effects that boosted the hydrogen storage performance of MgH₂.

Author Contributions: N.S., Writing—original draft, methodology; M.F.M.D., writing—review and editing; M.I., supervision, writing—original draft. All authors have read and agreed to the published version of the manuscript.

Funding: This study was supported by the Golden Goose Research Grant (GGRG) (VOT 55190) provided by Universiti Malaysia Terengganu.

Institutional Review Board Statement: Not applicable.

Informed Consent Statement: Not applicable.

Data Availability Statement: The data presented in this study are available on request from the corresponding author.

Acknowledgments: This work was financially supported by the Golden Goose Research Grant (GGRG) under grant number VOT 55190. N. Sazelee thankful to UMT for BUMT scholarship.

Conflicts of Interest: The authors declare no conflict of interest.

References

1. Xu, X.; Zhou, Q.; Yu, D. The future of hydrogen energy: Bio-hydrogen production technology. *Int. J. Hydrogen Energy* **2022**, *47*, 33677–33698. [[CrossRef](#)]
2. Wei, D.; Wei, P.; Li, D.; Ying, Z.; Hao, X.; Xue, Z. Intelligent damping control of renewable energy/hydrogen energy DC interconnection system. *Energy Rep.* **2022**, *8*, 972–982. [[CrossRef](#)]
3. Felderhoff, M.; Weidenthaler, C.; von Helmolt, R.; Eberle, U. Hydrogen storage: The remaining scientific and technological challenges. *Phys. Chem. Chem. Phys.* **2007**, *9*, 2643–2653. [[CrossRef](#)] [[PubMed](#)]
4. Simanullang, M.; Prost, L. Nanomaterials for on-board solid-state hydrogen storage applications. *Int. J. Hydrogen Energy* **2022**, *47*, 29808–29846. [[CrossRef](#)]
5. Liao, J.; Shao, Y.; Feng, Y.; Zhang, J.; Song, C.; Zeng, W.; Tang, J.; Dong, H.; Liu, Q.; Li, H. Interfacial charge transfer induced dual-active-sites of heterostructured $\text{Cu}_{0.8}\text{Ni}_{0.2}\text{WO}_4$ nanoparticles in ammonia borane methanolysis for fast hydrogen production. *Appl. Catal. B* **2023**, *320*, 121973. [[CrossRef](#)]
6. Feng, Y.; Li, Y.; Liao, Q.; Zhang, W.; Huang, Z.; Chen, X.; Youxiang, S.; Dong, H.; Liu, Q.; Li, H. Modulation the electronic structure of hollow structured $\text{CuO-NiCo}_2\text{O}_4$ nanosphere for enhanced catalytic activity towards methanolysis of ammonia borane. *Fuel* **2023**, *332*, 126045. [[CrossRef](#)]
7. Ali, N.A.; Sazelee, N.A.; Ismail, M. An overview of reactive hydride composite (RHC) for solid-state hydrogen storage materials. *Int. J. Hydrogen Energy* **2021**, *46*, 31674–31698. [[CrossRef](#)]
8. Yao, J.; Wu, Z.; Wang, H.; Yang, F.; Ren, J.; Zhang, Z. Application-oriented hydrolysis reaction system of solid-state hydrogen storage materials for high energy density target: A review. *J. Energy Chem.* **2022**, *74*, 218–238. [[CrossRef](#)]
9. Sazelee, N.; Ali, N.; Yahya, M.; Mustafa, N.; Halim Yap, F.; Mohamed, S.; Ghazali, M.; Suwarno, S.; Ismail, M. Recent advances on Mg–Li–Al systems for solid-state hydrogen storage: A Review. *Front. Energy Res.* **2022**, *10*, 875405. [[CrossRef](#)]
10. Wang, L.; Hu, Y.; Lin, J.; Leng, H.; Sun, C.; Wu, C.; Li, Q.; Pan, F. The hydrogen storage performance and catalytic mechanism of the $\text{MgH}_2\text{-MoS}_2$ composite. *J. Magnes. Alloy* **2022**, *in press*.
11. Liu, B.; Zhang, B.; Chen, X.; Lv, Y.; Huang, H.; Yuan, J.; Lv, W.; Wu, Y. Remarkable enhancement and electronic mechanism for hydrogen storage kinetics of Mg nano-composite by a multi-valence Co-based catalyst. *Mater. Today Nano* **2022**, *17*, 100168. [[CrossRef](#)]
12. Sazelee, N.A.; Idris, N.H.; Md Din, M.F.; Yahya, M.S.; Ali, N.A.; Ismail, M. LaFeO_3 synthesised by solid-state method for enhanced sorption properties of MgH_2 . *Results Phys.* **2020**, *16*, 102844. [[CrossRef](#)]
13. Zhang, L.; Nyahuma, F.M.; Zhang, H.; Cheng, C.; Zheng, J.; Wu, F.; Chen, L. Metal organic framework supported niobium pentoxide nanoparticles with exceptional catalytic effect on hydrogen storage behavior of MgH_2 . *Green Energy Environ.* **2021**, *in press*. [[CrossRef](#)]
14. Verma, S.K.; Shaz, M.A.; Yadav, T.P. Enhanced hydrogen absorption and desorption properties of MgH_2 with graphene and vanadium disulfide. *Int. J. Hydrogen Energy* **2022**, *in press*. [[CrossRef](#)]
15. Gao, S.; Liu, H.; Xu, L.; Li, S.; Wang, X.; Yan, M. Hydrogen storage properties of nano-CoB/CNTs catalyzed MgH_2 . *J. Alloys Compd.* **2018**, *735*, 635–642. [[CrossRef](#)]
16. Liu, G.; Qiu, F.; Li, J.; Wang, Y.; Li, L.; Yan, C.; Jiao, L.; Yuan, H. NiB nanoparticles: A new nickel-based catalyst for hydrogen storage properties of MgH_2 . *Int. J. Hydrogen Energy* **2012**, *37*, 17111–17117. [[CrossRef](#)]
17. Zhang, B.; Xie, X.; Wang, Y.; Hou, C.; Sun, X.; Zhang, Y.; Yang, X.; Yu, R.; Du, W. In situ formation of multiple catalysts for enhancing the hydrogen storage of MgH_2 by adding porous $\text{Ni}_3\text{ZnCo}_{0.7}/\text{Ni}$ loaded carbon nanotubes microspheres. *J. Magnes. Alloy* **2022**, *in press*. [[CrossRef](#)]
18. Zhou, D.; Cui, K.; Zhou, Z.; Liu, C.; Zhao, W.; Li, P.; Qu, X. Enhanced hydrogen-storage properties of MgH_2 by Fe–Ni catalyst modified three-dimensional graphene. *Int. J. Hydrogen Energy* **2021**, *46*, 34369–34380. [[CrossRef](#)]
19. Yao, P.; Jiang, Y.; Liu, Y.; Wu, C.; Chou, K.-C.; Lyu, T.; Li, Q. Catalytic effect of Ni@rGO on the hydrogen storage properties of MgH_2 . *J. Magnes. Alloy* **2020**, *8*, 461–471. [[CrossRef](#)]
20. Hou, Q.; Zhang, J.; Guo, X.; Yang, X. Improved MgH_2 kinetics and cyclic stability by fibrous spherical NiMoO_4 and rGO. *J. Taiwan Inst. Chem. Eng.* **2022**, *134*, 104311. [[CrossRef](#)]
21. Meng, Q.; Huang, Y.; Ye, J.; Xia, G.; Wang, G.; Dong, L.; Yang, Z.; Yu, X. Electrospun carbon nanofibers with in-situ encapsulated Ni nanoparticles as catalyst for enhanced hydrogen storage of MgH_2 . *J. Alloys Compd.* **2021**, *851*, 156874. [[CrossRef](#)]
22. Jalil, Z.; Rahwanto, A.; Handoko, E.; Akhyar, H. Hydrogen storage properties of mechanical milled MgH_2 -nano Ni for solid hydrogen storage material. *IOP Conf. Ser. Mater. Sci. Eng.* **2018**, *432*, 012034. [[CrossRef](#)]
23. Yu, Z.; Zhang, W.; Zhang, Y.; Fu, Y.; Cheng, Y.; Guo, S.; Li, Y.; Han, S. Remarkable kinetics of novel Ni@ $\text{CeO}_2\text{-MgH}_2$ hydrogen storage composite. *Int. J. Hydrogen Energy* **2022**, *47*, 35352–35364. [[CrossRef](#)]
24. Zhang, Y.; Zheng, J.; Lu, Z.; Song, M.; He, J.; Wu, F.; Zhang, L. Boosting the hydrogen storage performance of magnesium hydride with metal organic framework-derived Cobalt@Nickel oxide bimetallic catalyst. *Chin. J. Chem. Eng.* **2022**, *52*, 161–171. [[CrossRef](#)]
25. Yang, X.; Hou, Q.; Yu, L.; Zhang, J. Improvement of the hydrogen storage characteristics of MgH_2 with a flake Ni nano-catalyst composite. *Dalton Trans.* **2021**, *50*, 1797–1807. [[CrossRef](#)]
26. Yim, C.D.; You, B.S.; Na, Y.S.; Bae, J.S. Hydriding properties of Mg–xNi alloys with different microstructures. *Catal. Today* **2007**, *120*, 276–280. [[CrossRef](#)]

27. Fu, Y.; Zhang, L.; Li, Y.; Guo, S.; Yu, H.; Wang, W.; Ren, K.; Zhang, W.; Han, S. Effect of ternary transition metal sulfide FeNi_2S_4 on hydrogen storage performance of MgH_2 . *J. Magnes. Alloy* **2022**, *in press*. [[CrossRef](#)]
28. Tome, K.C.; Xi, S.; Fu, Y.; Lu, C.; Lu, N.; Guan, M.; Zhou, S.; Yu, H. Remarkable catalytic effect of Ni and ZrO_2 nanoparticles on the hydrogen sorption properties of MgH_2 . *Int. J. Hydrogen Energy* **2022**, *47*, 4716–4724. [[CrossRef](#)]
29. Liu, J.; Liu, Y.; Liu, Z.; Ma, Z.; Ding, Y.; Zhu, Y.; Zhang, Y.; Zhang, J.; Li, L. Effect of rGO supported NiCu derived from layered double hydroxide on hydrogen sorption kinetics of MgH_2 . *J. Alloys Compd.* **2019**, *789*, 768–776. [[CrossRef](#)]
30. Mao, J.; Guo, Z.; Yu, X.; Liu, H.; Wu, Z.; Ni, J. Enhanced hydrogen sorption properties of Ni and Co-catalyzed MgH_2 . *Int. J. Hydrogen Energy* **2010**, *35*, 4569–4575. [[CrossRef](#)]
31. Zhang, J.; Shan, J.; Li, P.; Zhai, F.; Wan, Q.; Liu, Z.; Qu, X. Dehydrogenation mechanism of ball-milled MgH_2 doped with ferrites (CoFe_2O_4 , ZnFe_2O_4 , MnFe_2O_4 and $\text{Mn}_{0.5}\text{Zn}_{0.5}\text{Fe}_2\text{O}_4$) nanoparticles. *J. Alloys Compd.* **2015**, *643*, 174–180. [[CrossRef](#)]
32. Polanski, M.; Bystrzycki, J. Comparative studies of the influence of different nano-sized metal oxides on the hydrogen sorption properties of magnesium hydride. *J. Alloys Compd.* **2009**, *486*, 697–701. [[CrossRef](#)]
33. El-Eskandarany, M.S. Metallic glassy $\text{Zr}_{70}\text{Ni}_{20}\text{Pd}_{10}$ powders for improving the hydrogenation/dehydrogenation behavior of MgH_2 . *Sci. Rep.* **2016**, *6*, 26936. [[CrossRef](#)] [[PubMed](#)]
34. Liao, W.; Jiang, W.; Yang, X.-S.; Wang, H.; Ouyang, L.; Zhu, M. Enhancing (de) hydrogenation kinetics properties of the Mg/ MgH_2 system by adding ANi_5 (A = Ce, Nd, Pr, Sm, and Y) alloys via ball milling. *J. Rare Earth* **2021**, *39*, 1010–1016. [[CrossRef](#)]
35. El-Eskandarany, M.S.; Saeed, M.; Al Nasrallah, E.; Al Ajmi, F.; Banyan, M. Effect of LaNi_3 amorphous alloy nanopowders on the performance and hydrogen storage properties of MgH_2 . *Energies* **2019**, *12*, 1005. [[CrossRef](#)]
36. Wu, C.; Wang, Y.; Liu, Y.; Ding, W.; Sun, C. Enhancement of hydrogen storage properties by in situ formed LaH_3 and Mg_2NiH_4 during milling MgH_2 with porous LaNiO_3 . *Catal. Today* **2018**, *318*, 113–118. [[CrossRef](#)]
37. Wei, S.; Qian, L.; Jia, D.; Miao, Y. Synthesis of 3D flower-like $\text{Ni}_{0.6}\text{Zn}_{0.4}\text{O}$ microspheres for electrocatalytic oxidation of methanol. *Electrocatalysis* **2019**, *10*, 540–548. [[CrossRef](#)]
38. Gogoi, P.; Saikia, B.J.; Dolui, S.K. Effects of nickel oxide (NiO) nanoparticles on the performance characteristics of the jatropha oil based alkyd and epoxy blends. *J. Appl. Polym. Sci.* **2015**, *132*, 41490. [[CrossRef](#)]
39. Rahdar, A.; Aliahmad, M.; Azizi, Y. NiO nanoparticles: Synthesis and characterization. *J. Nanostruct.* **2015**, *5*, 145–151.
40. Raja, K.; Ramesh, P.S.; Geetha, D. Structural, FTIR and photoluminescence studies of Fe doped ZnO nanopowder by co-precipitation method. *Spectrochim. Acta A Mol. Biomol. Spectrosc.* **2014**, *131*, 183–188. [[CrossRef](#)]
41. Handore, K.; Bhavsar, S.; Horne, A.; Chhattise, P.; Mohite, K.; Ambekar, J.; Pande, N.; Chabukswar, V. Novel green route of synthesis of ZnO nanoparticles by using natural biodegradable polymer and its application as a catalyst for oxidation of aldehydes. *J. Macromol. Sci. A* **2014**, *51*, 941–947. [[CrossRef](#)]
42. Bhunia, A.; Jha, P.; Rout, D.; Saha, S. Morphological properties and raman spectroscopy of ZnO nanorods. *J. Phys. Sci.* **2016**, *21*, 111–118.
43. Marinho, J.Z.; Romeiro, F.d.C.; Lemos, S.C.S.; Motta, F.V.d.; Riccardi, C.; Li, M.S.; Longo, E.; Lima, R.C. Urea-based synthesis of zinc oxide nanostructures at low temperature. *J. Nanomater.* **2012**, *2012*, 3. [[CrossRef](#)]
44. Bose, P.; Ghosh, S.; Basak, S.; Naskar, M.K. A facile synthesis of mesoporous NiO nanosheets and their application in CO oxidation. *J. Asian Ceram. Soc.* **2016**, *4*, 1–5. [[CrossRef](#)]
45. Bhatnagar, A.; Johnson, J.K.; Shaz, M.; Srivastava, O. TiH_2 as a dynamic additive for improving the de/rehydrogenation properties of MgH_2 : A combined experimental and theoretical mechanistic investigation. *J. Phys. Chem. C* **2018**, *122*, 21248–21261. [[CrossRef](#)]
46. Sazelee, N.A.; Idris, N.H.; Md Din, M.F.; Mustafa, N.S.; Ali, N.A.; Yahya, M.S.; Halim Yap, F.A.; Sulaiman, N.N.; Ismail, M. Synthesis of $\text{BaFe}_{12}\text{O}_{19}$ by solid state method and its effect on hydrogen storage properties of MgH_2 . *Int. J. Hydrogen Energy* **2018**, *43*, 20853–20860. [[CrossRef](#)]
47. Ali, N.A.; Idris, N.H.; Md Din, M.F.; Mustafa, N.S.; Sazelee, N.A.; Halim Yap, F.A.; Sulaiman, N.N.; Yahyaa, M.S.; Ismail, M. Nanolayer-like-shaped MgFe_2O_4 synthesised via a simple hydrothermal method and its catalytic effect on the hydrogen storage properties of MgH_2 . *RSC Adv.* **2018**, *8*, 15667–15674. [[CrossRef](#)]
48. Juahir, N.; Mustafa, N.; Sinin, A.; Ismail, M. Improved hydrogen storage properties of MgH_2 by addition of Co_2NiO nanoparticles. *RSC Adv.* **2015**, *5*, 60983–60989. [[CrossRef](#)]
49. Zhang, J.; He, L.; Yao, Y.; Zhou, X.; Yu, L.; Lu, X.; Zhou, D. Catalytic effect and mechanism of NiCu solid solutions on hydrogen storage properties of MgH_2 . *Renew. Energy* **2020**, *154*, 1229–1239. [[CrossRef](#)]
50. Luo, Q.; An, X.-H.; Pan, Y.-B.; Zhang, X.; Zhang, J.-Y.; Li, Q. The hydriding kinetics of Mg–Ni based hydrogen storage alloys: A comparative study on Chou model and Jander model. *Int. J. Hydrogen Energy* **2010**, *35*, 7842–7849. [[CrossRef](#)]
51. Cheng, B.; Kong, L.; Li, Y.; Wan, D.; Xue, Y. Hydrogen desorption kinetics of $\text{V}_{30}\text{Nb}_{10}(\text{Ti}_x\text{Cr}_{1-x})_{60}$ high-entropy alloys. *Metals* **2023**, *13*, 230. [[CrossRef](#)]
52. Wang, S.; Yong, H.; Yao, J.; Ma, J.; Liu, B.; Hu, J.; Zhang, Y. Influence of the phase evolution and hydrogen storage behaviors of Mg–RE alloy by a multi-valence Mo-based catalyst. *J. Energy Storage* **2023**, *58*, 106397. [[CrossRef](#)]
53. Lozano, G.A.; Ranong, C.N.; Bellosta von Colbe, J.M.; Bormann, R.; Fieg, G.; Hapke, J.; Dornheim, M. Empirical kinetic model of sodium alanate reacting system (I). Hydrogen absorption. *Int. J. Hydrogen Energy* **2010**, *35*, 6763–6772. [[CrossRef](#)]
54. Pang, Y.; Li, Q. A review on kinetic models and corresponding analysis methods for hydrogen storage materials. *Int. J. Hydrogen Energy* **2016**, *41*, 18072–18087. [[CrossRef](#)]

55. Zhang, J.; Yan, S.; Xia, G.; Zhou, X.; Lu, X.; Yu, L.; Yu, X.; Peng, P. Stabilization of low-valence transition metal towards advanced catalytic effects on the hydrogen storage performance of magnesium hydride. *J. Magnes. Alloys* **2020**, *9*, 647–657. [[CrossRef](#)]
56. Ali, N.A.; Yahya, M.S.; Sazelee, N.; Din, M.F.M.; Ismail, M. Influence of nanosized CoTiO₃ synthesized via a solid-state method on the hydrogen storage behavior of MgH₂. *Nanomaterials* **2022**, *12*, 3043. [[CrossRef](#)] [[PubMed](#)]
57. Chen, M.; Xiao, X.; Wang, X.; Lu, Y.; Zhang, M.; Zheng, J.; Chen, L. Self-templated carbon enhancing catalytic effect of ZrO₂ nanoparticles on the excellent dehydrogenation kinetics of MgH₂. *Carbon* **2020**, *166*, 46–55. [[CrossRef](#)]
58. Zhang, J.; Hou, Q.; Chang, J.; Zhang, D.; Peng, Y.; Yang, X. Improvement of hydrogen storage performance of MgH₂ by MnMoO₄ rod composite catalyst. *Solid State Sci.* **2021**, *121*, 106750. [[CrossRef](#)]
59. Hu, S.; Zhang, H.; Yuan, Z.; Wang, Y.; Fan, G.; Fan, Y.; Liu, B. Ultrathin K₂Ti₈O₁₇ nanobelts for improving the hydrogen storage kinetics of MgH₂. *J. Alloys Compd.* **2021**, *881*, 160571. [[CrossRef](#)]
60. Rafatnejad, M.; Raygan, S.; Sefidmooy Azar, M. Investigation of dehydrogenation performance and air stability of MgH₂-PMMA nanostructured composite prepared by direct high-energy ball-milling. *Mater. Renew. Sustain. Energy* **2020**, *9*, 14. [[CrossRef](#)]
61. Czujko, T.; Oleszek, E.E.; Szot, M. New aspects of MgH₂ morphological and structural changes during high-energy ball milling. *Materials* **2020**, *13*, 4550. [[CrossRef](#)] [[PubMed](#)]
62. Shahi, R.R.; Raghubanshi, H.; Shaz, M.; Srivastava, O. Studies on the de/re-hydrogenation characteristics of nanocrystalline MgH₂ admixed with carbon nanofibres. *Appl. Nanosci.* **2012**, *2*, 195–201. [[CrossRef](#)]
63. Somo, T.R.; Maponya, T.C.; Davids, M.W.; Hato, M.J.; Lototsky, M.V.; Modibane, K.D. A comprehensive review on hydrogen absorption behaviour of metal alloys prepared through mechanical alloying. *Metals* **2020**, *10*, 562. [[CrossRef](#)]
64. Nyahuma, F.M.; Zhang, L.; Song, M.; Lu, X.; Xiao, B.; Zheng, J.; Wu, F. Significantly improved hydrogen storage behaviors in MgH₂ with Nb nanocatalyst. *Int. J. Miner. Metall. Mater.* **2022**, *29*, 1788–1797. [[CrossRef](#)]
65. Maddah, M.; Rajabi, M.; Rabiee, S.M. Hydrogen desorption properties of nanocrystalline MgH₂-10 wt.% ZrB₂ composite prepared by mechanical alloying. *J. Ultrafine Grained Nanostruct. Mater.* **2014**, *47*, 21–26.
66. Xiao, X.; Liu, Z.; Saremi-Yarahmadi, S.; Gregory, D.H. Facile preparation of β-/γ-MgH₂ nanocomposites under mild conditions and pathways to rapid dehydrogenation. *Phys. Chem. Chem. Phys.* **2016**, *18*, 10492–10498. [[CrossRef](#)]
67. Zhang, Q.; Huang, Y.; Xu, L.; Zang, L.; Guo, H.; Jiao, L.; Yuan, H.; Wang, Y. Highly dispersed MgH₂ nanoparticle-graphene nanosheet composites for hydrogen storage. *ACS Appl. Nano Mater.* **2019**, *2*, 3828–3835. [[CrossRef](#)]
68. Ismail, M.; Zhao, Y.; Yu, X.; Dou, S. Improved hydrogen storage properties of MgH₂ doped with chlorides of transition metals Hf and Fe. *Energy Educ. Sci. Technol. A Energy Sci. Res.* **2012**, *30*, 107–122.
69. Zhang, J.; Hou, Q.; Guo, X.; Yang, X. Achieve high-efficiency hydrogen storage of MgH₂ catalyzed by nanosheets CoMoO₄ and rGO. *J. Alloys Compd.* **2022**, *911*, 165153. [[CrossRef](#)]
70. Zou, R.; Adedeji Bolarin, J.; Lei, G.; Gao, W.; Li, Z.; Cao, H.; Chen, P. Microwave-assisted reduction of Ti species in MgH₂-TiO₂ composite and its effect on hydrogen storage. *Chem. Eng. J.* **2022**, *450*, 138072. [[CrossRef](#)]
71. Huang, H.X.; Yuan, J.G.; Zhang, B.; Zhang, J.G.; Zhu, Y.F.; Li, L.Q.; Wu, Y. A noteworthy synergistic catalysis on hydrogen sorption kinetics of MgH₂ with bimetallic oxide Sc₂O₃/TiO₂. *J. Alloys Compd.* **2020**, *839*, 155387. [[CrossRef](#)]
72. Aguey-Zinsou, K.F.; Ares Fernandez, J.R.; Klassen, T.; Bormann, R. Using MgO to improve the (de)hydrogenating properties of magnesium. *Mater. Res. Bull.* **2006**, *41*, 1118–1126. [[CrossRef](#)]
73. Shan, J.; Li, P.; Wan, Q.; Zhai, F.; Zhang, J.; Li, Z.; Liu, Z.; Volinsky, A.A.; Qu, X. Significantly improved dehydrogenation of ball-milled MgH₂ doped with CoFe₂O₄ nanoparticles. *J. Power Sources* **2014**, *268*, 778–786. [[CrossRef](#)]
74. Ali, N.; Idris, N.; Din, M.M.; Yahya, M.; Ismail, M. Nanoflakes MgNiO₂ synthesised via a simple hydrothermal method and its catalytic roles on the hydrogen sorption performance of MgH₂. *J. Alloys Compd.* **2019**, *796*, 279–286. [[CrossRef](#)]
75. Zhang, J.; He, L.; Yao, Y.; Zhou, X.J.; Jiang, L.K.; Peng, P. Hydrogen storage properties of magnesium hydride catalyzed by Ni-based solid solutions. *Trans. Nonferrous Met. Soc. China* **2022**, *32*, 604–617. [[CrossRef](#)]
76. Patah, A.; Takasaki, A.; Szymid, J.S. The effect of Cr₂O₃/ZnO on hydrogen desorption properties of MgH₂. *Mater. Res. Soc. Symp. Proc.* **2009**, *1148*, 1148-PP03-38.

Disclaimer/Publisher's Note: The statements, opinions and data contained in all publications are solely those of the individual author(s) and contributor(s) and not of MDPI and/or the editor(s). MDPI and/or the editor(s) disclaim responsibility for any injury to people or property resulting from any ideas, methods, instructions or products referred to in the content.